## **ATOMIC PHYSICS**

# Atomic physics on a 50-nm scale: Realization of a bilayer system of dipolar atoms

Li Du\*+, Pierre Barral++, Michael Cantara+S, Julius de Hond¶, Yu-Kun Lu, Wolfgang Ketterle

Controlling ultracold atoms with laser light has greatly advanced quantum science. The wavelength of light sets a typical length scale for most experiments to the order of 500 nanometers (nm) or greater. In this work, we implemented a super-resolution technique that localizes and arranges atoms on a sub-50-nm scale, without any fundamental limit in resolution. We demonstrate this technique by creating a bilayer of dysprosium atoms and observing dipolar interactions between two physically separated layers through interlayer sympathetic cooling and coupled collective excitations. At 50-nm distance, dipolar interactions are 1000 times stronger than at 500 nm. For two atoms in optical tweezers, this should enable purely magnetic dipolar gates with kilohertz speed.

major frontier in many-body physics is the realization and study of strongly correlated quantum phases (1-3). In ultracold atomic systems, the typical short-range contact interaction has led to the creation of a variety of exotic quantum phases (3, 4). However, a wide range of quantum phenomena require long-range dipolar interactions (5-7). But even for the most magnetic atoms such as chromium, erbium, and dysprosium (Dy), the magnetic dipole-dipole interaction is rather weak. For Dy, with a magnetic dipole moment of 10 Bohr magneton ( $\mu_B$ ), the dipolar interaction at 500-nm distance is only  $h \times$ 20 Hz, where h is Planck's constant. Although such weak interactions could be observed (8, 9), and supersolidity and other forms of matter could be realized with magnetic atoms (5), there are major efforts to harness the much stronger interactions of polar molecules (10, 11) and Rydberg atoms (12). The electric dipolar interaction of molecules (at 3 D) can be 1000 times stronger than the magnetic dipolar interaction (at 10  $\mu_B$ ). In this work, we show how this factor of 1000 can be compensated for by decreasing the distance between two magnetic atoms to 50 nm. Studying dipolar physics with neutral atoms has major advantages: It is simpler to cool atoms to quantum degeneracy, and atoms have more favorable collisional properties.

It has been a long-standing goal to create optical potentials with subwavelength components to enhance tunneling and interaction strengths. Early works on atom lithography achieved deposition of metal structures with spatial periods one-eighth the size of optical wavelengths (13, 14) and feature sizes of tens

MIT-Harvard Center for Ultracold Atoms, Research Laboratory of Electronics, Department of Physics, Massachusetts Institute of Technology, Cambridge, MA 02139, USA.

\*Corresponding author. Email: lidu@mit.edu

†These authors contributed equally to this work. ‡Present address: Amazon Web Services, Boston, MA, USA. §Present address: Oracle Cloud Infrastructure, Boston, MA, USA. ¶Present address: PASQAL SAS, Fred. Roeskestraat 100, Amsterdam, Netherlands.

JSA. MA, USA

of nanometers (15) using state-dependent potentials. With ultracold atoms, many schemes have been suggested (16-20), and methods such as dark states (21, 22), radio frequencyphoton dressing (23), stroboscopic techniques (24), and multiphoton processes through Raman transitions between hyperfine states (13, 25, 26) have been demonstrated. Challenges, such as additional heating, limited coherence time, and limited reduction of atomic spacing, have hindered a wide adoption of these methods. In this work, we introduce a method that has no fundamental limit. It is based on the key concept of optical super-resolution microscopy: One can determine the center of a diffractionlimited Airy disk with a precision that exceeds the diffraction limit. Similarly, a deep optical lattice or a strong tweezer beam can localize an atom to 10 nm (15, 27, 28), limited only by available power and heating from spontaneous light scattering. In a typical super-resolution microscopy experiment, molecules are imaged sequentially, whereas for trapping atoms, simultaneous confinement on a subwavelength scale is required. One possible solution is to trap two different kinds of atoms with two different colors of light. But, usually, for quantum science, one needs identical atoms. The strategy we implemented was to use two opposite spin states of Dy and two different polarizations of light at different frequencies-a dual-polarization and dual-frequency superresolution scheme. Unlike spin-1/2 and alkali atoms, ground-state Dy has a strong tensor polarizability (29). It can cause detrimental two-photon Raman couplings between spin states with different  $m_I$  quantum numbers, which are suppressed by the frequency offset between the two optical potentials. The remaining diagonal part of the tensor couplings makes our scheme much more robust because it creates, for  $^{162}\mathrm{Dy},$  an isolated two-state Hilbert space for  $m_I = \pm 8$  spin states with a big energy gap to all the other 15 spin states.

Spin-dependent potentials have been realized with rubidium (30–34) and cesium (27, 35). In

contrast to alkali atoms (36), very deep s dependent potentials can be realized with with negligible spontaneous emission as a result of Dy's electronic orbital angular momentum in the ground state. Furthermore, with a magnetic dipole moment of only 1  $\mu_B$ , the dipolar interaction for alkali atoms is 100 times weaker than for Dy. Therefore, previous work on alkalis has used spin-dependent forces to control the overlap between sites with spin up and down (27, 33) but not to study interactions between nonoverlapping sites.

#### The subwavelength scheme

An illustration of the experimental scheme is shown in Fig. 1B, which demonstrates a bilayer potential created by two optical standing waves of  $\sigma_+$  and  $\sigma_-$  polarizations with a small spatial displacement s. This illustration also applies to the case of spin-dependent optical tweezers. The figure shows the adiabatic potentials of all 17 spin states (quantized along the z direction in the lab frame), with different polarizability components taken into account. With only a scalar polarizability  $\alpha_z$ , the ac Stark shifts are the same for all 17  $m_J$ states, so there is only one potential minimum. The vector polarizability  $\alpha_n$  leads to ac Stark shifts that are linear in  $m_I$  and therefore can be regarded as a Zeeman shift caused by a fictitious sinusoidal magnetic field-it lifts the degeneracy except for points where the fictitious magnetic fields from the  $\sigma_+$  and the  $\sigma_$ standing waves cancel. This creates a doublewell potential even for an arbitrarily small displacement of the standing waves. However, small transverse magnetic fields would couple the degenerate states, leading to mixing among different  $m_I$  states. This is where the tensor polarizability  $\alpha_t$  makes a qualitative difference. The diagonal part of the tensor light-atom interaction (which has an  $m_I^2$  dependence) partially lifts the degeneracy. The  $m_J = \pm 8$  ground states are separated from all other states by a large gap and are coupled by transverse fields only in 16th order. Note that the  $m_J = \pm 8$  states are the local ground states of the  $\sigma_{\pm}$  potential minima, and therefore inelastic two-body losses are prevented in each of the layers.

Although the tensor polarizability  $\alpha_t$  provides robustness against transverse magnetic fields, it allows for two-photon Raman processes with  $\Delta m_J = \pm 2$  using one  $\sigma_+$  and one  $\sigma_-$  photon. Figure 1C shows the effect of the resonant Raman process caused by off-diagonal tensor couplings when both polarization components have the same frequency. This is the situation when the  $\sigma_+$  and the  $\sigma_-$  standing waves are created by retroreflecting a single beam with rotated linear polarization, as often used for alkalis [e.g., see (30,31,33)]. For Dy, the Raman couplings weaken the potential minima for separations smaller than  $\lambda/10$ , where  $\lambda$  is the wavelength of the light. For

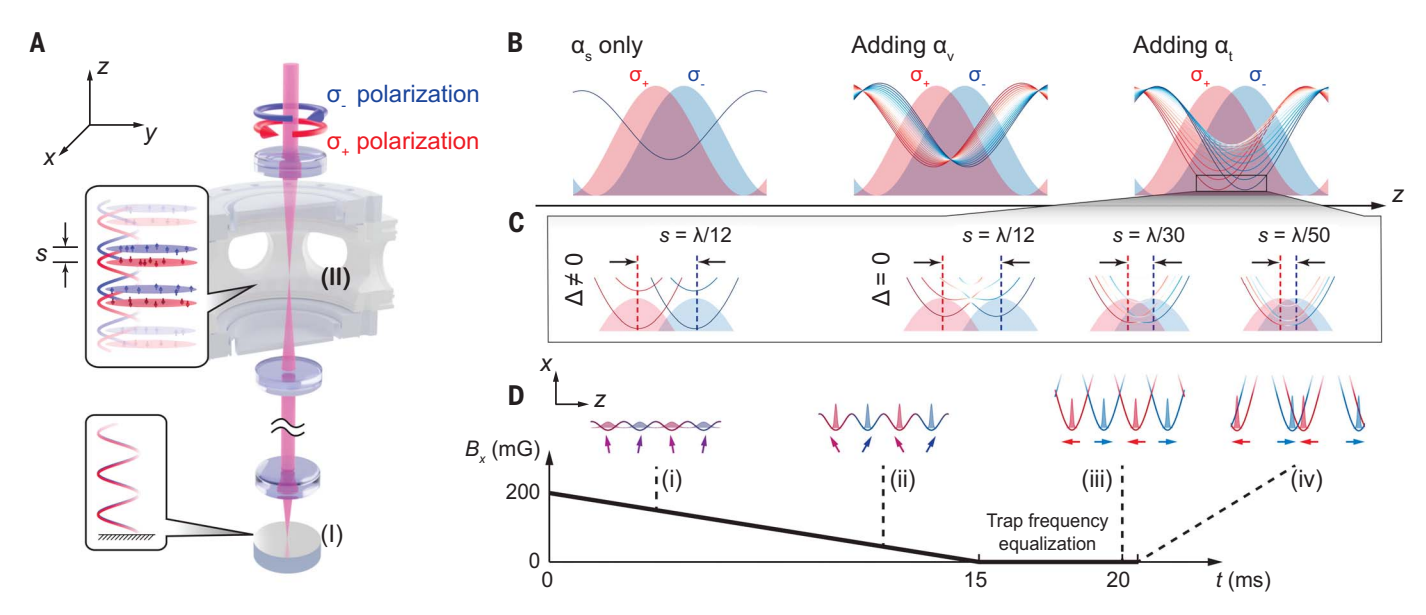


**Fig. 1. Creation of the subwavelength bilayer array.** (**A**) Experimental setup. Two overlapping laser beams with opposite circular polarizations  $\sigma_+$  and  $\sigma_-$  are retroreflected by a mirror (I) to form two optical standing waves. The two standing waves are displaced at the position of the atoms (II), which is controlled by the frequency offset  $\Delta$  between the two laser beams. Dy atoms in this configuration form an array of pancake-shaped bilayers of head-to-head dipoles with adjustable interlayer distance s. (**B**) Contributions of different polarizability components. Solid lines denote adiabatic potential curves for different  $m_J$  states ( $-8 \le m_J \le 8$ , represented by dark blue to dark red, assuming red detuning), and the shaded regions refer to the intensities of the  $\sigma_\pm$  light for a particular interlayer separation. (**C**) If the two laser beams have the same

frequency  $\Delta=0$ , the off-diagonal part of the tensor polarizability mixes spin states. As a result, the two minima merge into a single minimum for a small separation s. This is avoided in our experiment by using two different frequencies for the  $\sigma_{\pm}$  light. The color of the curves indicate the  $m_J$  character of the adiabatic eigenstates. (**D**) Adiabatic loading of the bilayer array. (i) Starting with the optical potential in the interlaced configuration in the presence of a dominating transverse magnetic field  $B_x=200$  mG, the atoms are initialized in the  $m_J=-8$  spin state along the x direction. (ii) As  $B_x$  is ramped down in 15 ms, the light shift dominates over the Zeeman shift, thereby adiabatically loading the bilayer array. (iii) The power of the  $\sigma_+$  and  $\sigma_-$  potentials is adjusted for identical trap frequencies. (iv) The interlayer distance is adjusted to designated values in 0.5 ms.

displacements of the standing waves of less than  $\lambda/30$ , the double minima have merged. We eliminated the Raman coupling by offsetting the frequencies for the  $\sigma_+$  and  $\sigma_-$  optical standing waves by more than 300 MHz, much larger than the ac Stark shifts, which makes the two-photon Raman process off-resonant (37). The conclusion is that the dual-polarization and dual-frequency scheme isolates the Hilbert space for the  $m_J=\pm 8$  spin states and creates a double-minimum potential that is not flattened out even for very small separations of the two minima.

Dy, with its high angular momentum of J=8 in the ground state, is the ideal atom for this scheme. For  $aJ=8 \rightarrow J'=9$  transition, the  $m_J=8$  state has a transition strength ratio of 153 between the  $\sigma_+$  and  $\sigma_-$  transitions (38). For atoms with J=1 (2), the ratio is only 6 (15). Therefore, this stretched transition in Dy is very similar to a hypothetically isolated  $J=1/2 \rightarrow J'=1/2$  transition, where the spin-up state sees only  $\sigma_-$  light and vice versa. Dy is even more ideal than the J=1/2 case in which spin-up and down states are directly connected by possible one- or two-body couplings (e.g., transverse magnetic fields, dipolar relaxation), whereas those couplings act only in 16th

or 8th order in our Dy scheme. The robustness of the scheme comes from the ac Stark shifts that stem from the tensor polarizability.

## **Experimental protocol**

Experimentally, we created a stack of bilayers by superimposing red-detuned optical standing waves with  $\sigma_+$  and  $\sigma_-$  polarizations operating near the Dy narrowline transition at 741 nm (linewidth  $\Gamma/2\pi=1.78$  kHz) (39). The two optical beams were delivered through the same polarization-maintaining fiber, such that they shared the same transverse Gaussian mode. The frequency of the  $\sigma_-$  standing wave can be dynamically tuned using a double-passed phased-array acousto-optic deflector, leading to a precise control of the interlayer distance s with a sensitivity of 4.7 nm MHz<sup>-1</sup> (40).

The ground state of the bilayer was loaded using an adiabatic transfer method, as depicted in Fig. 1D. First,  $m_J = -8$  atoms were prepared in a magnetic field with a transverse component  $B_x = 200$  mG and an axial component  $B_z$  around 10 mG. We then ramped up the  $\sigma_+$  and  $\sigma_-$  standing waves in the interlaced configuration with  $s = \lambda/4$  in 100 ms, loading all layers with atoms aligned with the x axis (Fig. 1D, i). By ramping down  $B_x$  in

15 ms, the potential depth increased while a bilayer array was formed with dipoles aligned head to head (Fig. 1D, ii and iii). We ensured balanced loading by making sure that the energy offset (including Zeeman energies) between the minima of the  $\sigma_+$  and  $\sigma_-$  potentials was zero. It was crucial that the atoms stayed in their local ground state throughout the experiment to prevent losses and heating caused by dipolar relaxation. Therefore, the Zeeman shifts caused by the external magnetic field  $B_z$  had to be smaller than the differential ac Stark shift between the  $m_J=-8$  and  $m_J=-7$  states.

After loading a balanced bilayer array, the powers of the two optical standing waves were ramped up, ensuring that the two layers had the same trap frequencies of typically  $(\omega_x, \omega_y, \omega_z) = 2\pi \times (0.5, 0.5, 140)$  kHz. The strong axial confinement resulted in a harmonic oscillator length  $a_{\rm HO} = \sqrt{h/m\omega_z}$  of 21.1 nm, where  $\hbar = h/2\pi$  and m is the atomic mass. We loaded  $4.2 \times 10^4$  ultracold  $^{162}$ Dy atoms into an array of 42 bilayers, with a temperature of 1.7  $\mu$ K determined from the cloud size after ballistic expansion (40, 41). Subsequently, the interlayer distance s was ramped from  $\lambda/4$  to different designated values in 0.5 ms by changing

Fig. 2. Subwavelength control of the interlayer distance, as demonstrated by recording atom loss as a function of layer separation.

(A) Evolution of the population in  $\sigma_+$  layers at two different interlayer distances s of 185 and 0 nm. The loss is much faster when the layers are overlapped. Initial loss rates  $\Gamma_{3b}$  are obtained from the fits to the decay curves. (B) Gaussian fits of the initial loss rates  $\Gamma_{3b}$  to the interlayer distances s according to Eq. 1 (solid lines) provide a value of  $\sigma_z=19\pm1$  nm for the layer thickness.

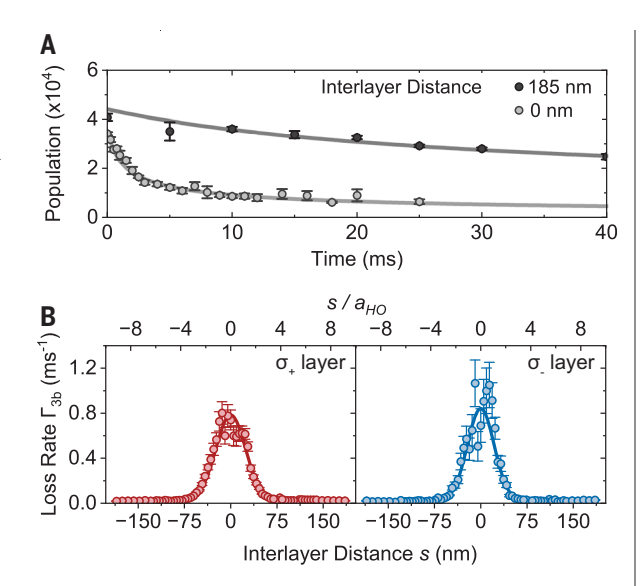
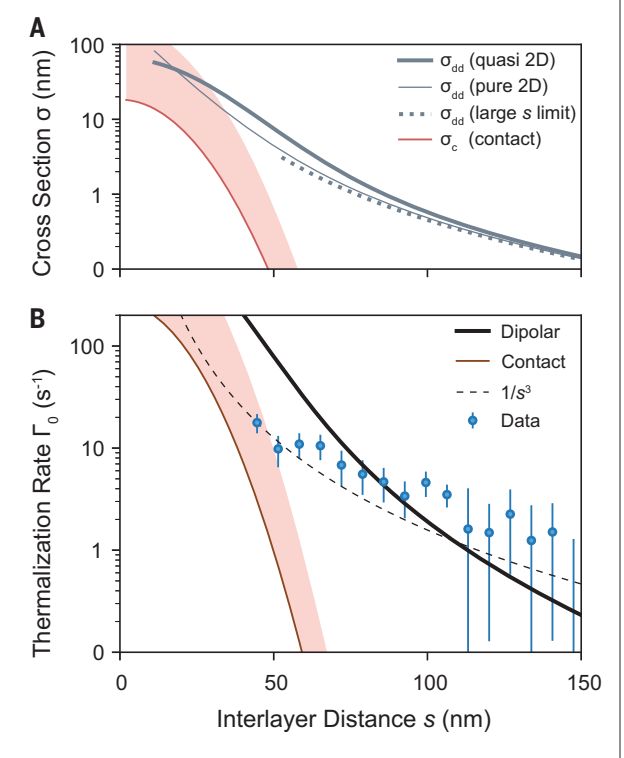


Fig. 3. Observation of interlayer thermalization. (A) Interlayer elastic scattering cross sections as functions of separation s calculated using the Born approximation. The gray curves correspond to dipolar cross sections for infinitely thin  $\sigma_z = 0$  layers (thin gray) along with its large interlayer distance limit ks>1 (dashed gray, following Eq. 2) and for layers with finite thickness  $\sigma_z$  = 14.9 nm (quasi-2D, solid gray). The red curve is for simple contact interactions at the background scattering length (red, quasi 2D), and the shaded area corresponds to a 10-times-enhanced cross section. (B) Observed thermalization rates  $\Gamma_0$  obtained from the pseudo-exponential fits. The black and red solid lines show the expected thermalization rate from dipolar and contact interactions (40). The dashed line is for reference and is proportional to 1/s<sup>3</sup>. Error bars represent the standard errors of the rates obtained from the pseudo-exponential fits.



the frequency of the  $\sigma_-$  standing wave. The interlayer distance s was calibrated with Kapitza-Dirac diffraction measurements (40). At the end of each experimental sequence, the atoms were released from the bilayer array within 1  $\mu$ s and were imaged after ballistic expansion. With the small axial magnetic field  $B_z$  serving as a guiding field, atoms remained in the  $m_J$  =  $\pm 8$  states and were imaged by a spin-resolved absorption imaging technique (40). This meth-

od allowed us to measure the population in each of the two lavers simultaneously.

## **Demonstration of spatial control**

We demonstrated the subwavelength spatial control over the bilayer geometry by measuring the lifetime of atomic samples at different layer separations. The sharp peak in the loss rate as a function of interlayer distance s in Fig. 2 is essentially the convolution between

the density profiles of the two layers. Assuming that loss processes occur at short range, we derived a rate equation for the total loss rate  $\Gamma_{3b}$  of each layer

$$\Gamma_{3\mathrm{b}} = \Gamma_{\mathrm{intra}} + \Gamma_{\mathrm{inter}} e^{-\frac{1}{3} \left(\frac{s}{\sigma_z}\right)^2} = \frac{\dot{N}_{\mathrm{tot}}}{N_{\mathrm{tot}}}$$
 (1)

where  $N_{\rm tot}$  is the total number of atoms in a layer and  $\sigma_z$  is the root-mean-square thickness of each laver. The loss rate contains both an intra- and interlayer contribution characterized by  $\Gamma_{intra}$  and  $\Gamma_{inter}$  The factor of one-third in the exponent of the interlayer term reflects that the loss is caused by three-body recombination (40). For spin-independent three-body collisions and thermal clouds, we expect that  $\Gamma_{intra}$  =  $\Gamma_{inter}.$  Unexpectedly, we observed about a 50-fold increase in the loss rate when the two layers were overlapped, which implies that three-body recombination involving mixed spin states is much faster than recombination of three atoms that are all in the same spin state. This strongly enhanced loss feature serves as a highly sensitive monitor for the density overlap between the two layers; fitting the loss curve determines the thickness of each layer  $\sigma_z = 19 \pm 1$  nm, consistent with the calculated value of  $1.31a_{\rm HO}/\sqrt{2}\approx18.8\pm0.1\,\rm nm$  that we obtained from trap frequency and temperature measurements (41). The observed losses in the two layers are almost equal, which implies equal loss rates for three-body collisions involving one spin-up and two spin-down atoms, or vice versa. This measurement of the atomic density distribution has no discernible broadening: The measured and calculated widths agreed to within 1 nm. Expressing this as an instrumental point spread function gives an upper limit to the Gaussian width of the pointspread function of 6 nm. This result can be compared with what was achieved in dark-state super-resolution microscopy. McDonald et al. (22) measured an atom cloud size of 55 nm with a broadening of 32 nm due to the width of the dark-state probe. A similar experiment reported by Subhankar et al. (42) measured a size of 26 nm with a broadening of 11 nm from the probe.

We conclude from the loss measurement that the two layers can be regarded as coupled predominantly by long-range dipolar forces for  $s \gtrsim 50$  nm. The dipolar energy  $U_{\rm dd}/h$  between two Dy atoms with opposite spins at this separation is 20 kHz. This geometry now allows us to study physics with strong interlayer dipole-dipole interactions.

## Interlayer thermalization

We applied our technique to study energy transfer through interlayer dipolar interactions, or sympathetic cooling between two atomic systems separated by vacuum (43, 44). Each layer receives heat through the fluctuating magnetic field created by the dipoles in the other layer. For equal temperatures, in detailed

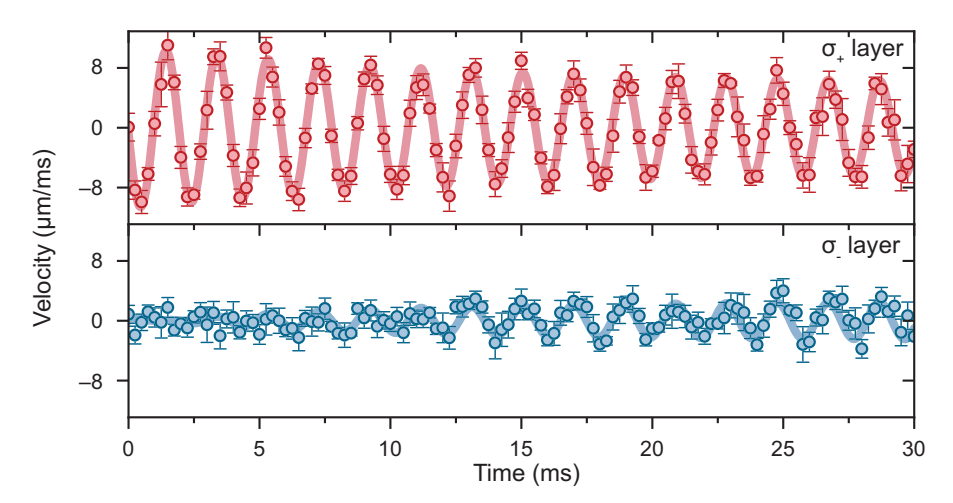


Fig. 4. Observation of coupled oscillations of the two layers at a 62-nm interlayer distance. The center-of-mass oscillation of the  $\sigma_+$  layer is excited by suddenly switching off a displacement force. The  $\sigma_-$  layer oscillates because of dipolar coupling. Error bars represent the standard errors of the means of independent measurements.

balance, the heat flows cancel. For unequal temperatures, the dipolar fluctuations cause thermalization. Figure 3B shows the experimental results.

We experimentally created a controlled temperature difference between the two layers by heating up the  $\sigma_+$  layer using a parametric drive by modulating the  $\sigma_+$  light intensity at twice the transverse trap frequency for 30 ms, followed by a 5-ms hold to ensure any residual breathing motion is damped out. This procedure prepares the  $\sigma_+$  layer at 3.9  $\mu K$  and leaves the  $\sigma_{-}$  layer at 1.7  $\mu$ K. We then adjusted the interlayer distance over 0.5 ms and monitored the temperature evolution. We fit the temperature difference between two layers to a pseudo-exponential decay  $\frac{\mathrm{d}\Delta T}{\mathrm{d}t}=-\Gamma_0\frac{N(t)}{N(0)}\Delta T$  to obtain the interlayer thermalization rate  $\Gamma_0$ , where N(t) accounts for the measured particle number decay caused by inelastic collisions (40). Figure 3B shows that the thermalization rate strongly drops with interlayer distance.

We could estimate the interlayer collision rate as  $n_{\rm 2D}\sigma_{\rm dd}v_{\rm rel}$ , where  $n_{\rm 2D}$  is the 2D density distribution and  $\sigma_{\rm dd}$  is the cross section for two dipolar atoms passing each other at a separation s. Using the Born approximation (45–48), we calculated the elastic cross section between two atoms in thin layers separated by a distance s (40), and the analytic large-s limit is

$$\sigma_{\rm dd}^{\rm 2D} = a_{\rm dd}^2 \frac{\pi}{k^2 s^3} \tag{2}$$

Here,  $a_{\rm dd}=10.2$  nm is the dipolar length and k is the relative momentum between the colliding particles. For s=75 nm, the quasi-2D cross section  $\sigma_{\rm dd}$  is 0.38 nm (see Fig. 3A). With a typical 2D peak density of  $n_{\rm 2D}\approx 1.3\times 10^9~{\rm cm}^{-2}$  and a thermal velocity of 2.1 cm s $^{-1}$  one obtains

an interlayer collision rate of 100 s<sup>-1</sup>. The observed thermalization times are much slower, around 160 ms (rate of  $6 \text{ s}^{-1}$ ). This can be fully accounted for by the anisotropy of dipolar scattering peaked in the forward direction, which reduces the effective cross section by a factor of six, and by multiple averaging arising from the inhomogeneity of our sample (40). In Fig. 3B, we compare the observed thermalization rates to calculations (40). They do not have any adjustable parameters and fully take into account the momentum and angular dependence of dipolar scattering and the finite thickness of the layer. The calculations are in semiquantitative agreement with the observations. The drop-off of the thermalization rate is much weaker than the steep exponential decrease in density overlap and, therefore, in the contact interactions between the two layers. This is clear evidence for purely dipolar couplings in the range of 50- to 100-nm interlayer distances.

The observed dependence on s roughly follows a  $1/s^3$  dependence, which is less steep than predicted. This is possibly a consequence of the assumption of purely dipolar binary collisions. For small s, there can be an interference term with s-wave contact interactions and a contribution from nonuniversal shortrange dipolar s-wave scattering (49), which is not included in the Born approximation. The largest separations s studied are comparable to the interparticle separation, and the binary collision approximation may no longer be accurate; that is, there are now more than two particles interacting with each other.

#### Coupled collective oscillations

In the second experiment, we looked for coupled collective oscillations of the bilayer system. Several theoretical papers (50, 51) predicted the coupling of transverse oscillations by the mean dipolar field between the layers. Indeed, when we excited transverse oscillations in one layer, we found that they caused oscillations in the other layer (Fig. 4). Experimentally, after loading a balanced bilayer array and adjusting the interlayer distance to a designated value in 0.5 ms, we adiabatically displaced the  $\sigma_+$  layer along the transverse direction y in 10 ms using an extra laser beam with  $\sigma_+$  polarization. This beam, blue-detuned from the 626-nm transition by 458 MHz, is misaligned from the atoms by about one beam waist and displaces the atoms only in the  $\sigma_+$  layer (40). A sudden switch-off of this beam hence creates a center-of-mass oscillation of the  $\sigma_+$  layer at the transverse trap frequency with an adjustable amplitude ranging from 0 to 8 µm, depending on the final power of the beam. As a function of hold time, we obtained the in-trap velocity of each layer from time-of-flight images to reveal how momentum is transferred between layers.

Figure 4 shows the time evolution of the velocity of each layer at s = 62 nm, as obtained from ballistic expansion images. The harmonic oscillation of the  $\sigma_{\perp}$  layer shows damping, whereas the  $\sigma_{-}$  layer starts at rest and shows a growing in-phase oscillation. Our observation contrasts with the theoretical treatments (50, 51), where the mean-field coupling potential would cause a beat note, which is initially an oscillation 90° out of phase. Furthermore, the predicted mean-field coupling (50, 51) resulted in a normal-mode splitting of less than 1 Hz, which is too slow to be observed on the experimental timescale. Our observation is fully consistent with a friction force caused by dipolar collisions: The time constant for the damping of the relative motion between the two layers of 25 ms is similar to the observed interlayer thermalization times. These observations establish dipolar drag between two physically separated layers, which have features in common with Coulomb drag studied in bilayer semiconductors (52).

#### **Discussion and outlook**

We expect that the technique we developed here should work for all atoms that have electronic orbital angular momentum in the ground state and allow strong vector and tensor ac Stark shifts at sufficiently far detuning. Although it requires the two layers to be in different spin states, those states can be tilted by a transverse magnetic field to angles within 20°. A modified scheme with an in-plane quantization axis could realize attractive interactions and interlayer pairing (47, 53).

Looking ahead, lower temperatures should lead to strong correlations between the layers beyond a mean-field description. Adding transverse optical lattices to the layers will create large repulsive interaction energies between

pairs on the same lattice site (7) but can also realize a system described by attractive interactions between particles and holes analogous to electron-hole pairs in bilayer excitons (54). It is possible to project separate arbitrary potentials into the  $\sigma_+$  and  $\sigma_-$  layers, which could realize twisted bilayer potentials (55) and more general geometries, including quasi-crystals. These geometries should allow the study of many phenomena that have been predicted for interacting bilayers (7, 50, 51, 56-62). Applying the super-resolution technique to optical tweezers will allow the study of super-radiance and radiative shifts at separations much smaller than the optical wavelength as well as the study of magnetic interactions and spin exchange between two isolated atoms, which was done recently with polar molecules (63-66). The tweezer setup can be generalized to a linear array of atoms alternating in spin-up and spindown states. Moving the spin-up atoms back and forth would provide full connectivity along the chain and realize a spin chain with strong magnetic coupling between nearest neighbors. These ideas can be generalized to higher dimensions.

#### REFERENCES AND NOTES

- 1. B. Keimer, J. Moore, Nat. Phys. 13, 1045-1055 (2017).
- E. Y. Andrei, A. H. MacDonald, Nat. Mater. 19, 1265–1275 (2020).
- M. Lewenstein, A. Sanpera, V. Ahufinger, Ultracold Atoms in Optical Lattices: Simulating Quantum Many-Body Systems (Oxford Univ. Press, 2012).
- I. Bloch, J. Dalibard, W. Zwerger, Rev. Mod. Phys. 80, 885–964 (2008).
- 5. L. Chomaz et al., Rep. Prog. Phys. 86, 026401 (2022).
- T. Lahaye, C. Menotti, L. Santos, M. Lewenstein, T. Pfau, Rep. Prog. Phys. 72, 126401 (2009).
- M. A. Baranov, M. Dalmonte, G. Pupillo, P. Zoller, Chem. Rev. 112, 5012–5061 (2012).
- 8. S. Müller et al., Phys. Rev. A 84, 053601 (2011).
- 9. S. Baier et al., Science 352, 201-205 (2016).
- B. Gadway, B. Yan, J. Phys. At. Mol. Opt. Phys. 49, 152002 (2016).
- S. A. Moses, J. P. Covey, M. T. Miecnikowski, D. S. Jin, J. Ye, Nat. Phys. 13, 13–20 (2017).
- 12. A. Browaeys, T. Lahaye, Nat. Phys. 16, 132-142 (2020).
- R. Gupta, J. J. McClelland, R. J. Celotta, P. Marte, *Phys. Rev. Lett.* 76, 4689–4692 (1996).
- 14. T. Schulze et al., Microelectron. Eng. 46, 105-108 (1999).
- C. C. Bradley, W. R. Anderson, J. J. McClelland, R. J. Celotta, Appl. Surf. Sci. 141, 210–218 (1999).
- 16. L. Caldwell, M. R. Tarbutt, Phys. Rev. Lett. 125, 243201 (2020).
- 17. L. Caldwell, M. Tarbutt, *Phys. Rev. Res.* **3**, 013291 (2021).

- M. Łącki, M. A. Baranov, H. Pichler, P. Zoller, *Phys. Rev. Lett.* 117, 233001 (2016).
- S. Nascimbene, N. Goldman, N. R. Cooper, J. Dalibard, Phys. Rev. Lett. 115, 140401 (2015).
- 20. A. Kruckenhauser et al., Phys. Rev. A 102, 023320 (2020).
- 21. Y. Wang et al., Phys. Rev. Lett. **120**, 083601 (2018).
- M. McDonald, J. Trisnadi, K.-X. Yao, C. Chin, *Phys. Rev. X* 9, 021001 (2019).
- 23. N. Lundblad et al., Phys. Rev. Lett. 100, 150401 (2008).
- T.-C. Tsui, Y. Wang, S. Subhankar, J. V. Porto, S. L. Rolston, *Phys. Rev. A* 101, 041603 (2020).
- G. Ritt, C. Geckeler, T. Salger, G. Cennini, M. Weitz, *Phys. Rev. A* 74, 063622 (2006).
- 26. R. P. Anderson et al., Phys. Rev. Res. 2, 013149 (2020).
- 27. L. Förster et al., Phys. Rev. Lett. 103, 233001 (2009).
- A. M. Kaufman, B. J. Lester, C. A. Regal, *Phys. Rev. X* 2, 041014 (2012).
- 29. Spin-1/2 atoms and alkalis for detunings larger than the excited-state hyperfine splitting share the property that they have only a scalar and vector polarizability. In general, atoms have a vector or tensor polarizability when light scattering can change their angular momentum by ħ or 2ħ, respectively (67, 68).
- 30. O. Mandel et al., Phys. Rev. Lett. 91, 010407 (2003).
- 31. B.-B. Yang et al., Phys. Rev. A 96, 011602 (2017).
- 32. P. Soltan-Panahi et al., Nat. Phys. 7, 434–440 (2011).
- 33. J. de Hond et al., Phys. Rev. Lett. 128, 093401 (2022).
- B. Gadway, D. Pertot, R. Reimann, D. Schneble, *Phys. Rev. Lett.* 105, 045303 (2010).
- 35. N. Belmechri et al., J. Phys. At. Mol. Opt. Phys. 46, 104006 (2013).
- 36. D. McKay, B. DeMarco, New J. Phys. 12, 055013 (2010).
- 37. If the Raman couplings are eliminated using an external magnetic field, it breaks the symmetry of the  $m_J$  = ±8 states and causes rapid dipolar relaxation in the  $m_J$  = ±8 layer.
- Depending on detuning, this contrast does not fully translate into the ac Stark shift because of the scalar background polarizability that is due to the strong transition triplet at 421, 419, and 405 nm.
- 39. M. Lu, S. H. Youn, B. L. Lev, Phys. Rev. A 83, 012510 (2011).
- 40. Materials and methods are available as supplementary materials.
- 41. For technical reasons, the lifetime measurements presented in Fig. 2 are done at trap frequencies of  $(\omega_x, \omega_y, \omega_z) = 2\pi \times (0.7, 0.7, 153)$  kHz and temperature of  $T = 5.5 \,\mu\text{K}$ . This leads to an oscillator length of  $a_{\text{HO}} = 20.2 \,$  nm and a layer thickness of

$$\frac{\sum_{n=0}^{\infty} (2n+1)e^{-n\hbar\omega_{n}/k_{B}T}}{\sum_{n=0}^{\infty} e^{-n\hbar\omega_{k}/k_{B}T}} \frac{1}{\sqrt{2}} = \sqrt{\coth\left(\frac{\hbar\omega_{n}}{2k_{B}T}\right)} \frac{1}{\sqrt{2}} \approx \frac{1}{\sqrt{2}}$$

- $1.31a_{HO}/\sqrt{2} \approx 18.8 \pm 0.1$  nm, where  $k_B$  is the Boltzmann constant, owing to thermal excitation into the higher axial vibrational levels.
- S. Subhankar, Y. Wang, T.-C. Tsui, S. L. Rolston, J. V. Porto, Phys. Rev. X 9, 021002 (2019).
- 43. B. Renklioglu, B. Tanatar, M. Oktel, *Phys. Rev. A* **93**, 023620 (2016).
- 44. C. Charalambous, M. A. Garcia-March, M. Mehboudi,
- M. Lewenstein, New J. Phys. 21, 083037 (2019).
- 45. S. Hensler *et al.*, *Appl. Phys. B* **77**, 765–772 (2003).
- 46. J. L. Bohn, D. S. Jin, Phys. Rev. A 89, 022702 (2014).
- M. A. Baranov, A. Micheli, S. Ronen, P. Zoller, *Phys. Rev. A* 83, 043602 (2011).
- 48. B. Pasquiou et al., Phys. Rev. A 81, 042716 (2010).
- S. Ronen, D. C. Bortolotti, D. Blume, J. L. Bohn, *Phys. Rev. A* 74, 033611 (2006).
- N. Matveeva, A. Recati, S. Stringari, Eur. Phys. J. D 65, 219–222 (2011)

- 51. C.-C. Huang, W.-C. Wu, Phys. Rev. A 82, 053612 (2010).
- J. A. Seamons, C. P. Morath, J. L. Reno, M. P. Lilly, *Phys. Rev. Lett.* 102, 026804 (2009).
- A. Pikovski, M. Klawunn, G. V. Shlyapnikov, L. Santos, *Phys. Rev. Lett.* 105, 215302 (2010).
- 54. J. P. Eisenstein, A. H. Macdonald, Nature 432, 691-694 (2004).
- 55. Z. Meng et al., Nature 615, 231-236 (2023).
- C. Trefzger, C. Menotti, M. Lewenstein, *Phys. Rev. Lett.* **103**, 035304 (2009).
- 57. A. Argüelles, L. Santos, *Phys. Rev. A* 75, 053613 (2007).
- D.-W. Wang, M. D. Lukin, E. Demler, *Phys. Rev. Lett.* 97, 180413 (2006).
- 59. P. Köberle, G. Wunner, Phys. Rev. A 80, 063601 (2009).
- A. Macia, G. Astrakharchik, F. Mazzanti, S. Giorgini, J. Boronat, Phys. Rev. A 90, 043623 (2014).
- D. Hufnagl, R. E. Zillich, Phys. Rev. A 87, 033624 (2013).
- 62. A. Safavi-Naini, Ş. G. Söyler, G. Pupillo, H. R. Sadeghpour, B. Capogrosso-Sansone, New J. Phys. 15, 013036 (2013).
- C. M. Holland, Y. Lu, L. W. Cheuk, Science 382, 1143–1147 (2023).
- 64. Y. Bao et al., Science 382, 1138-1143 (2023).
- 65. L. Christakis et al., Nature **614**, 64-69 (2023).
- 66. B. Yan et al., Nature 501, 521-525 (2013).
- F. Le Kien, P. Schneeweiss, A. Rauschenbeutel, *Eur. Phys. J. D* 67, 92 (2013).
- X. Cui, B. Lian, T.-L. Ho, B. L. Lev, H. Zhai, *Phys. Rev. A* 88, 011601 (2013).
- L. Du et al., Data for "Atomic physics on a 50 nm scale: Realization of a bilayer system of dipolar atoms." Zenodo (2023); https://doi.org/10.5281/zenodo.10689742.

#### **ACKNOWLEDGMENTS**

We thank A. Jamison, J. Yang, J. Lyu, and T. De Coninck for experimental assistance and discussions and J. Xiang and A. Jamison for comments on the manuscript, Funding: We acknowledge support from the NSF through grant nos. 1506369 and PHY-2208004, the Center for Ultracold Atoms (an NSF Physics Frontiers Center) through grant no. PHY-1734011, a Vannevar-Bush Faculty Fellowship (grant no. N00014-16-1-2815), and an Army Research Office (ARO) Defense University Research Instrumentation Program (DURIP) grant (no. W911NF-22-1-0024). Author contributions: L.D., P.B., and M.C. designed and constructed the experimental setup; L.D., P.B., M.C., J.d.H., and Y.-K.L. carried out the experimental work. W.K. initiated the work. All authors contributed to the development of models, data analysis, and writing of the manuscript. Competing interests: None declared. Data and materials availability: Data and code needed to evaluate the conclusions in this paper are available at Zenodo (69). License information: Copyright © 2024 the authors, some rights reserved; exclusive licensee American Association for the Advancement of Science. No claim to original US government works. https://www science.org/about/science-licenses-journal-article-reuse

# SUPPLEMENTARY MATERIALS

science.org/doi/10.1126/science.adh3023 Supplementary Text Figs. S1 to S4 References (70–81)

Submitted 23 February 2023; resubmitted 19 July 2023 Accepted 19 March 2024

10.1126/science.adh3023